

Shear-velocity structure of the crust and upper mantle beneath the Tibetan Plateau and southeastern China

Lian-She Zhao, Donald V. Helmberger and David G. Harkrider

Seismological Laboratory, California Institute of Technology, Pasadena, CA 91125, USA

Accepted 1991 January 11. Received 1991 January 11; in original form 1989 May 23

SUMMARY

This paper addresses the velocity structure of the crust and upper mantle beneath southern China with special emphasis on the Tibet region. Waveform data from 48 earthquakes as recorded on the WWSSN and GDSN are used in this detailed forward modelling study. Constraints on the upper crustal section are derived from modelling local Love waves in the time domain applying the mode-sum modelling technique. Lower crustal constraints are derived by modelling the P_{nl} -wavetrain with the reflectivity method. An average crustal thickness of 70 km is obtained beneath the Tibetan Plateau with a modest increase of velocity with depth. The lithospheric and upper mantle structure is deduced from modelling S and SS triplication waveform data and relative traveltimes by applying a combination of WKB and generalized ray methods. S – SS seismograms chosen with bounce-points directly under Tibet allow remote sensing of this inaccessible region. The resulting model is an averaged 1-D model where corrections for lateral variation have been applied. We conclude that the upper mantle structure in the entire region is basically shield-like below 200 km (SNA). However, the velocity of the lithosphere is abnormally slow, roughly 5 per cent beneath Tibet. The model for Tibet derived does not have a distinct lid, and has a positive velocity gradient in the crust, suggesting crustal shortening. A preliminary velocity model for southeastern China is also suggested.

Key words: shear velocity structure, southeastern China, Tibetan Plateau, upper mantle.

INTRODUCTION

China is a part of the Eurasian plate, but the margins of the Indian and Philippine plates are involved in the Himalayas and in the coastal ranges of Taiwan, respectively. Relative to the north of China, the Indian plate is moving NNE, and the Philippine plate is moving NW (Minster *et al.* 1974). The arrows in Fig. 1 show the directions of the motions of the plates surrounding China (Wang & Xu 1985). China is composed mainly of four major tectonic provinces, the Tarim Basin, Sino-Korea Craton, Yangtze Craton and the Tibetan Plateau. The Tarim basin, Sino-Korea Craton, and northern part of Yangtze Craton are pre-Cambrian massifs (Yang, Cheng & Wang 1986; Zhang, Liou & Coleman 1984). The provinces are characterized by large variations in crustal thickness as indicated in the isopach map presented in Fig. 2. The thickness of the crust of the eastern part of China is about 35 km, that of northern China is 45 km, and that of the Tibetan Plateau is more than 50 km. Thus, we would expect the crustal and upper mantle velocity

distributions beneath these four tectonic provinces to be very different.

The dynamic processes that lead to the formation and maintenance of a mean elevation of 5 km over the Tibetan Plateau are not well understood and are controversial. Because of its obvious importance for constraining these deep processes, the seismic velocity structure of the Tibetan Plateau has been the subject of many studies.

The three-year Sino-Franco joint research program (1980–1982) contributed significantly to both the geology and geophysics of the Tibetan Plateau. The P -wave velocity profile of a 600 km line (from 28.5°N, 89.0°E to 32.2°N, 91.7°E) was obtained from seismic soundings. The thickness of the crust changes from about 40 km to 75 km along this profile. The results of the program are published in a series of papers (see for example Hirn *et al.* 1984; Teng 1987).

Some studies of the seismic velocity structure of the Tibetan Plateau used group and phase velocities of fundamental mode surface waves (e.g. Chen & Molnar 1981; Romanowicz 1982, 1984; Brandon & Romanowicz

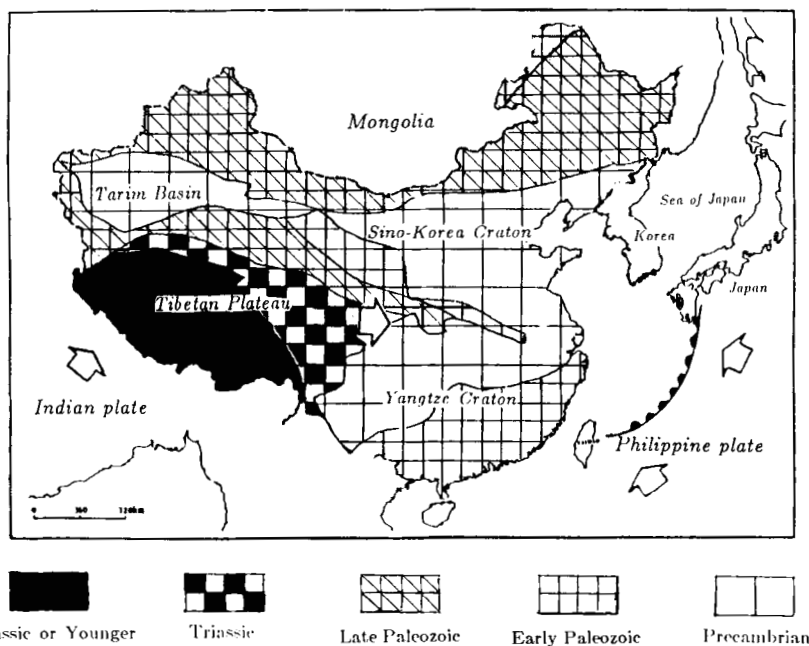


Figure 1. Sketch map of plate tectonics of China, and the directions of the motions of the plates surrounding China. China occupies the Eurasian plate, part of the Indian plate, and a small part of the Philippine Sea plate (Zhang *et al.* 1984).

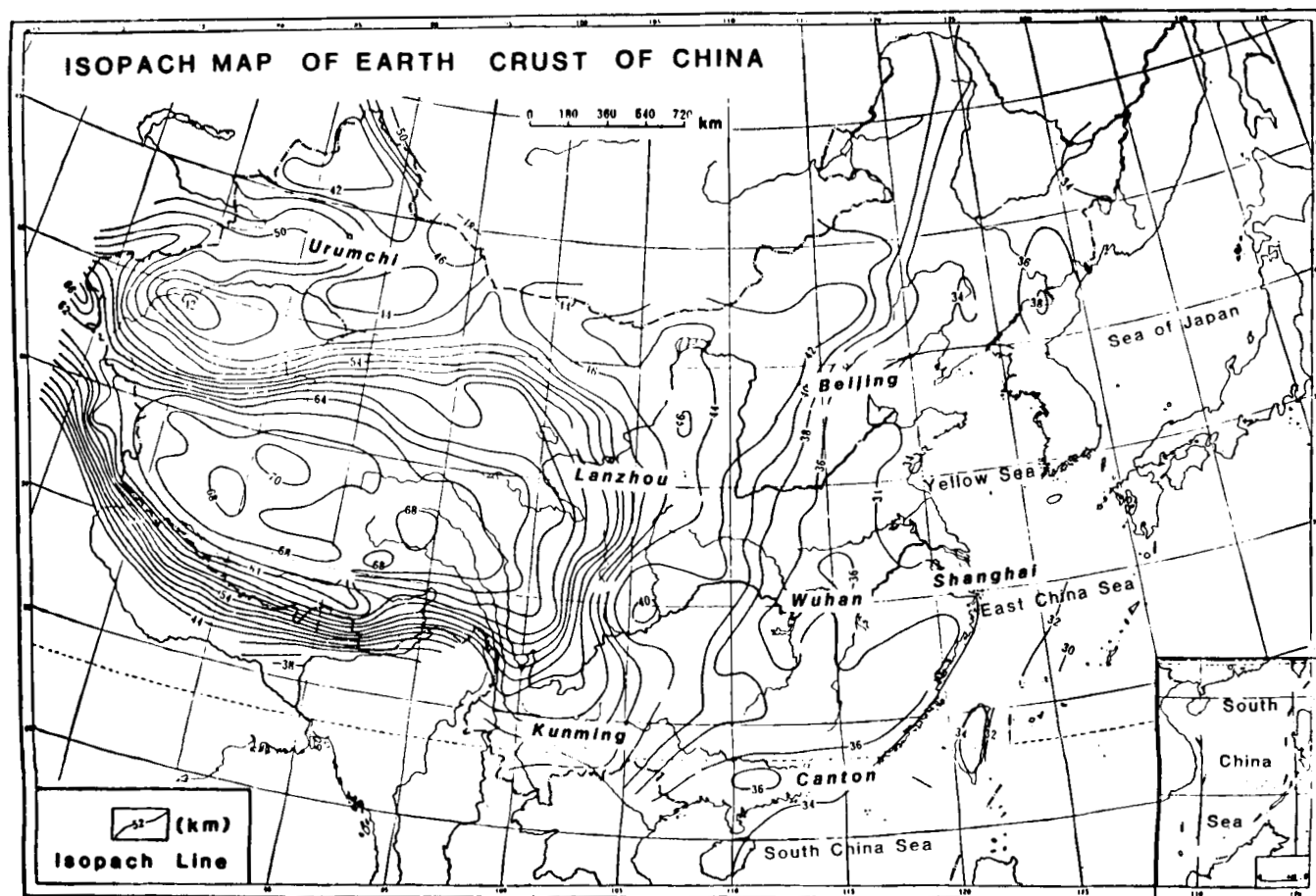


Figure 2. Isopach map showing crustal thickness (in kilometres, Zhang *et al.* 1984) in China. In eastern China, a distinct north–northeast-trending belt that contains a marked difference in crustal thickness is parallel to a subduction zone to the east of the Asian continent. The crustal thickness in western China, the Tibetan Plateau is more than 50 km.

1986; Feng 1982). Other studies used *Pn*- and *Sn*-waves (Barazangi & Ni 1982; Ni & Barazangi 1983; Holt & Wallace 1990) to derive the velocity of the lid beneath the crust of the plateau. Recently, Lyon-Caen (1986) used the traveltimes and waveforms of long-period *SH*-wave data recorded at distances of 10°–30° and some *SS*–*S* waveforms to constrain the upper mantle velocities down to a depth of 400 km beneath the plateau. She argues that the Indian plate is not underthrusting the whole of the Tibetan Plateau at the present time.

For the other parts of China, there are fewer studies reported in English. For the Yangtze Craton, there are surface wave studies (Wier 1982; Feng 1982). Shedlock & Roecker (1987) used traveltime inversion to study the elastic wave velocity structure of the crust and upper mantle beneath the Sino–Korea craton.

Wang & Yao (1989) gave one upper mantle shear velocity model for the Tibetan Plateau, and one upper mantle shear velocity model for North China (Tarim basin and Sino–Korea craton) by modelling the long-period *SS*–*S* waveforms recorded at distances of 30°–60°.

The purpose of this study is to constrain the upper mantle shear velocity structure of southern China by using the traveltimes and waveforms of Love waves recorded at distances of 7°–23°; long-period *S*-waves recorded at distances of 15°–30°; and long-period *SS*–*S*-waves recorded at distances of 30°–60°. Recent work using long-period body wave data have demonstrated that the traveltimes and waveforms of *SH*-waves recorded at distances up to 30° and of *SS*–*S*-waves recorded between 30° and 60° can provide some constraints on the large-scale velocity structure of the upper 670 km of the mantle and particularly of the upper 400 km (Grand & Helmberger 1984a, b; Rial, Grand & Helmberger 1984). In this distance range the waveforms are controlled by the interference of phases whose turning points are in the regions above the 400 km discontinuity, between the 400 and 670 km discontinuities, and below the 670 km discontinuity. The differential traveltimes of *SS*-waves and *S*-waves are controlled mainly by the velocity structure of the neighbourhood of the bounce-points of the *SS* phases. This property makes it possible to constrain the shear velocity structure of an area not big enough for the pure path data. The search of models can be achieved by comparing the synthetics with the data. The WKBJ method (Chapman 1978), which is discussed at length by Grand & Helmberger (1984a), was used for constructing synthetic *S*- and *SS*-waves, and the mode summation method (Harkrider 1964, 1970) was used in studying Love waves.

DATA AND METHODS

In this study, we used traveltimes and waveforms of long-period *SH*-wave data from 48 earthquakes, magnitude 4.5 or larger, from 1965 to 1985, within or around China (Table 1), as recorded at the WWSSN stations around China (ANP, BAG, HKC, KBL, LAH, MAT, MSH, NDI, NIL, QUE, SEO, SHL, SHK), SRO stations (KAAO, TATO), and some Chinese stations (GYA, GZH, LZH, XAN). In Table 1, the source information is from Bulletin of the International Seismological Centre (ISC), unless otherwise indicated. The seismograms have high signal-to-noise ratios, and are not necessarily from earthquakes with known source

Table 1. Earthquakes and stations used in this study.

	Date	Origin Time	Location (°N °E)	Depth (km)	Mag Mb Ms	Study area	Station	Δ	Phase
1	06 14 65	13 17.02.4	32.09 87.72	36	5.2	TP	SHL	7.5	Love
2	06 16 65	23.49.08.2	32.04 87.46	69	4.8	TP	NDI	9.5	Love
3	06 17 65	20 14.50.1	32.12 87.76	15	5.1	TP	LAH	11.4	Love
4	06 18 65	01.18.39.0	32.01 87.59	43	5.1	TP	NDI	9.6	Love
5	02 05 66	15.12.32.9	26.22 103.21	32	5.6	EC	SEO	23.1	S
6	02 07 66	23.06.37.4	30.25 69.89	28	5.6	TP	ANP	45.7	SS
7	03 14 66	04.42.50.7	32.47 97.46	33	4.8	TP	SHL	8.4	Love
8	03 17 66	05.44.47.9	31.60 82.76	11	4.7	TP	SHL	17.8	Love
9	03 29 66	06.12.00.8	37.52 114.99	33	5.3	EC	SHL	10.0	Love
10	09 28 66	14.00.21.0	27.53 100.08	12	5.7	TP	MSH	23.0	S
11	03 14 67	06.58.04.4	28.41 94.29	12	5.8	EC	HKC	35.3	SS
							ANP	19.0	S
							SHK	24.5	S
							MAT	33.2	SS
12	08 15 67	09.21.03.3	31.05 93.56	10	5.5	TP	SHL	37.7	SS
13	08 30 67	11.08.50.0	31.57 100.31	8	4.9	TP	NDI	20.2	Love ¹
14	09 15 67	10.32.44.2	27.42 91.86	19	5.8	EC	SHK	22.9	Love
15	12 22 68	09.06.35.0	36.25 101.83	21	5.5	TP	KBL	35.7	SS
16	10 17 69	01.25.11.5	23.09 94.70	124	6.1	EC	SHK	26.7	S
							MAT	35.0	SS
17	06 05 70	04.53.07.4	42.48 78.71	24	5.9 6.8	TP	HKC	39.7	SS
18	07 30 70	00.52.20.3	37.85 55.94	22	5.7	TP	HKC	35.7	SS
19	04 03 71	04.49.03.1	32.16 94.99	27	5.6 6.4	EC	MAT	52.0	SS
20	05 31 71	05.13.58.6	25.22 96.51	22	5.2 6.1	EC	MAT	35.7	SS
21	07 22 72	16.41.02.1	31.38 91.41	17	5.4 5.8	TP	NIL	37.3	SS
							QUE	15.5	S
22	08 30 72	15.14.7.5	36.65 96.35	17	5.5 5.5	TP	NDI	21.0	S
23	08 30 72	18.47.40.3	36.56 96.35	16	5.5 5.3	TP	QUE	17.9	Love
24	02 07 73	16.06.25.8	31.50 100.33	8	5.9	TP	NDI	25.3	S
							NIL	20.2	Love ¹
25	03 18 75	18.44.16.3	35.12 86.54	31	5.1 5.8	TP	QUE	22.9	Love
26	05 05 75	05.18.46.3	33.13 92.84	8	5.6 6.1	TP	NIL	17.2	S
27	10 03 75	17.31.35.6	30.44 66.41	24	5.5 6.4	TP	ANP	16.4	S
28	04 08 76	02.40.23.9	40.31 63.72	10	6.2 6.4	TP	ANP	48.6	SS
							HKC	50.0	SS
29	05 31 76	05.08.30.0	24.37 98.62	25	5.5 6.2	EC	ANP	46.0	SS
							MAT	20.8	S
30	05 31 76	18.35.05.0	24.29 98.68	20	5.1 5.5	EC	MAT	36.0	SS
31	07 03 78	08.46.32.0	32.75 94.08	8	4.7 4.9	TP	NDI	35.9	SS
31a	01 10 79	01.26.04.4	26.55 60.95	4	5.5 5.9	TP	TATO	15.1	Love
31b	01 16 79	09.50.06.9	33.96 59.53	10	5.9 6.7	TP	TATO	54.1	SS
32	03 15 79	12.52.26.0	23.18 101.09	6	5.5 6.2	EC	MAT	54.0	SS
33	05 20 79	22.59.11.6	29.93 80.27	16	5.7 5.7	TP	XAN	34.6	SS
33a	07 09 79	10.57.22.0	31.45 119.24	10	5.4 5.7	TP	KAAO	24.6	S
34	01 12 80	15.31.40.0	33.58 57.26	14	5.3 5.8	TP	HKC	41.9	SS
35	02 13 80	22.09.30.8	36.47 76.86	74	6.0 5.4	TP	GYA	51.0	SS
							ANP	27.2	S
36	02 22 80	03.02.43.7	30.66 88.65	10	6.0 5.4	TP	NDI	39.7	SS ²
							NIL	10.1	P _n
37	07 29 80	12.23.07.7	29.34 81.21	3	5.7 5.5	TP	LZH	13.4	P _n
							XAN	20.1	S
37a	03 02 81	12.13.46.2	22.88 121.47	28	5.4 6.2	TP	KAAO	24.0	SS
38	01 23 82	17.37.29.2	31.68 82.28	25	6.0 6.5	TP	LZH	47.0	SS
39	06 15 82	23.24.28.8	31.85 99.92	7		TP	NDI	18.4	S
40	04 18 83	10.58.49.1	27.78 62.07	44	6.4 6.3	TP	SEO	20.2	Love ¹
							HKC	54.5	SS
41	12 16 83	13.15.57.3	39.34 72.96	35	5.7 5.9	TP	BAG	59.7	SS
42	02 01 84	14.22.09.2	34.57 70.48	44	5.9 5.9	TP	ANP	47.2	SS
							TATO	44.8	SS
43	10 26 84	20.22.21.8	39.15 71.35	7	5.9 6.2	TP	HKC	44.9	SS
							ANP	40.1	SS
44	10 29 85	13.13.40.0	36.75 54.81	13	6.0 6.0	TP	GZH	44.2	SS
								51.8	SS

Holt & Wallace (1989); ² this study. TP—Tibetan Plateau; EC—eastern China.

mechanisms. There are only a limited number of Tibetan earthquakes carefully studied (e.g. Ni & Barazangi 1984; Molnar & Chen 1983; Tapponnier & Molnar 1977; Baranowski *et al.* 1984). Because of lack of local station net, it is almost impossible to know the source mechanisms of the smaller Tibetan earthquakes, which generated on-scale surface waves. However, we can infer roughly the source mechanism from the *S*-waveforms (Langston & Helmberger 1975). This rough source mechanism is sufficient for *S*- and *SS*-wave study as demonstrated by Grand & Helmberger (1985). The source depth effects on *S*- and *SS*-waveforms are corrected for by using teleseismic *S*-waveforms as the source time history since the ray parameter changes very slowly with distance for distances greater than 15.0°. The orientation of the fault affects the amplitude ratio of *SS*- to *S*-waves, which was not used. These various approximations have been used in previous *SS*–*S* studies; see for example Rial *et al.* (1984).

The crustal velocity structure has not been well determined in the Tibetan Plateau. To constrain this portion of the model we used relatively high-frequency Love waves. But instead of applying the conventional dispersion analysis, we chose to match the Love wave synthetics to the

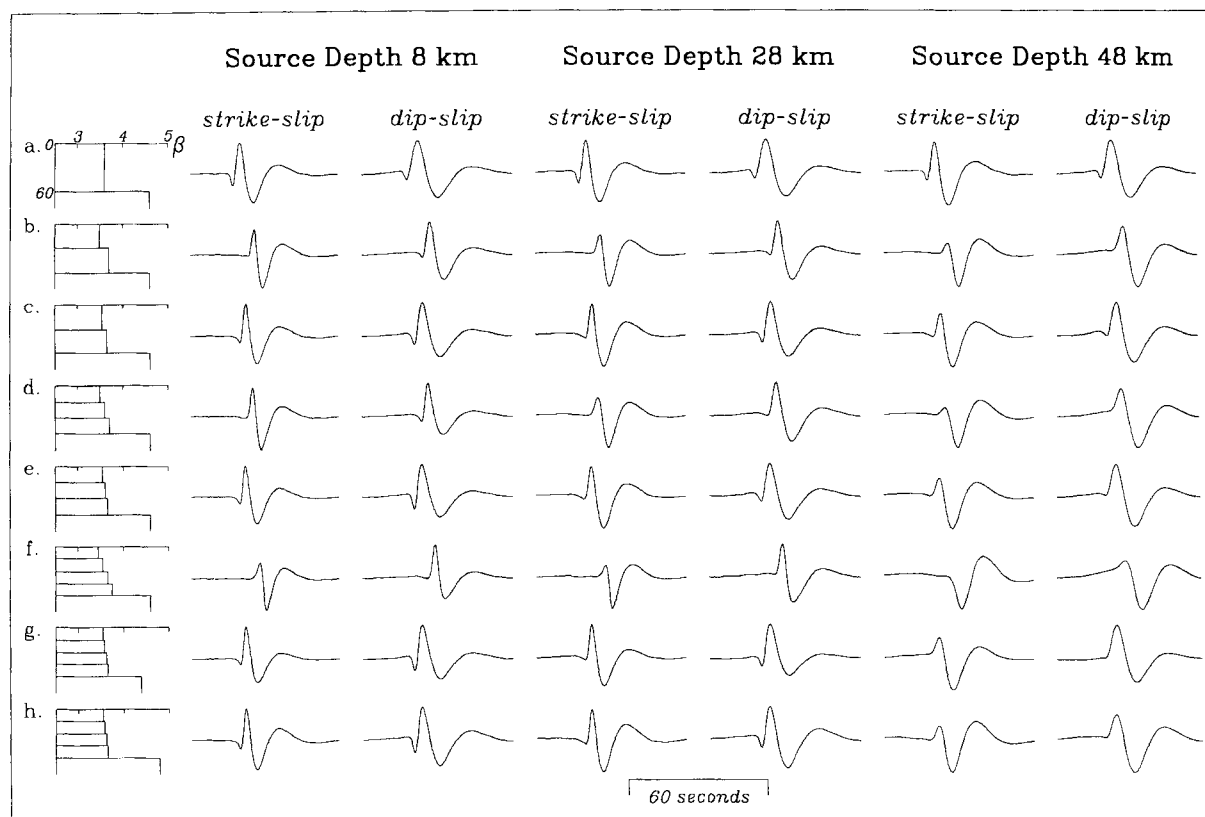


Figure 3. Fundamental Love wave synthetics for a variety of models, source mechanisms, and depths. The column on the left shows the models used to generate the synthetics on the right. The crustal thickness is 60 km, and the average velocity of the crust is 3.6 km s^{-1} . The velocity of the mantle is 4.6 km s^{-1} , except for models g, 4.4 km s^{-1} , and h, 4.8 km s^{-1} . The distance is 1000 km, and the source function is a trapezoid (1, 1, 1).

observations directly. The appropriateness of the model is then judged on the overall fit of the synthetics to the observed waveform in absolute traveltimes.

Since Love wave data are not normally used in this fashion, we start with a brief sensitivity study to test the resolving power of this approach by discussing some numerical experiments. Figs 3 and 4 summarize the results of these numerical experiments. Fig. 3 shows the sensitivity of synthetics to changes in the models, source depths, and source mechanisms. Fig. 4 displays the synthetics appropriate for different Moho discontinuities.

In Fig. 3, the left column shows the models used to generate the synthetics of fundamental Love waveforms at various depths and mechanisms. These synthetics were generated at a distance of 1000 km, assuming the source time history of a (1, 1, 1) trapezoid. All synthetics begin at 260 s. The crustal thickness is 60 km for all models. The average velocities of the crust are the same; 3.6 km s^{-1} . The mantle velocities are the same, 4.6 km s^{-1} , except model g which is 4.4 km s^{-1} and h which is 4.8 km s^{-1} . The attenuation, Q_β , used is 300 for the crust, and 1000 for the mantle. Comparing the synthetics for these various sensitivities we conclude that: the mantle velocity has very little effect on both traveltimes and waveforms (see the synthetics of models g and h); the velocity of the upper crust seems to dominate the traveltimes of Love waves (see models b, c, f and g); the velocity gradient does not have much

effect on waveforms; the source depth has a profound effect on the waveforms for complicated crustal models, and less effect for simpler models; the source mechanism affects traveltimes only weakly compared to shallow velocity structure.

Figure 4 displays some properties of regional Love waves when crossing a plateau boundary similar to the expected geometry of the Tibetan Plateau. The column on the left displays the source-receiver geometry in a simple idealized crust where all the models have the velocities given at the bottom. The distance is set at 1000 km, and a strike-slip source is assumed at a depth of 9.8 km. These synthetics were generated with generalized ray theory and a finite-difference method; see Helmberger & Vidale (1988). The Love waveforms are quite similar which lead us to conclude that the lower crustal parameters are rather insignificant. Thus, regional Love waveforms can be used as a constraint on the velocity structure of the upper crustal layers for paths crossing the plateau with the above restrictions on geometry.

RESULTS

The upper mantle shear velocity structures we derived are given in Table 2 and Fig. 5. TIP is the model for the Tibetan Plateau, and ECH that for the eastern part of China, part of Yangtze and Sino-Korean Cratons.

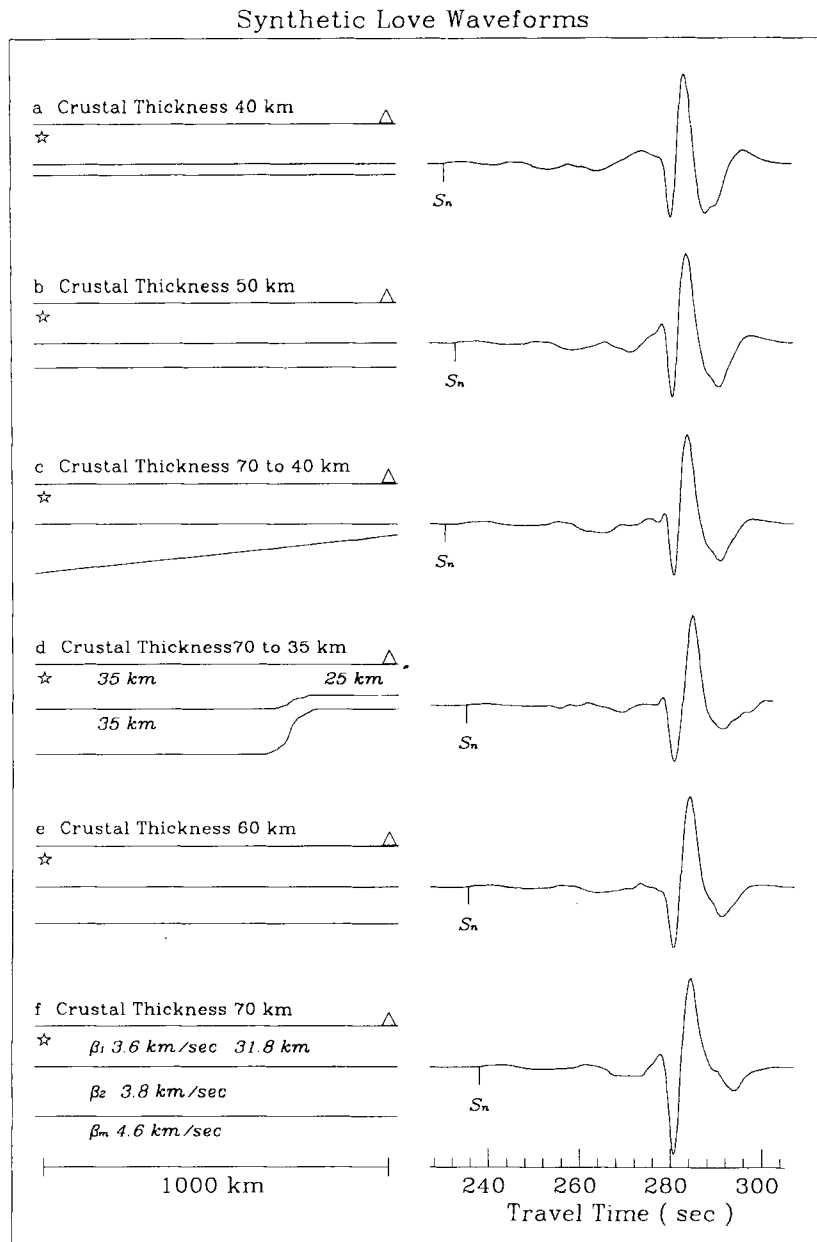


Figure 4. A comparison of Love wave synthetics for different models. The column on the right displays the synthetics derived from the models on the left. The models are of a two-layer crust over a half-space mantle. The shear velocity of the upper layer is 3.6 km s^{-1} , that of the lower layer is 3.8 km s^{-1} , and that of the mantle is 4.6 km s^{-1} . Except for model d, the models have a 31.8 km thick upper crust. The star is the source, and the triangle is the receiver. A strike-slip source, with a Gaussian time history, halfwidth 1.26 s , is used. The source depth is 9.8 km , distance is 1000 km .

Tibetan Plateau

It is convenient to break this discussion into two sections, namely the crust and upper mantle, where the former is constrained by regional long-period Love waves and the latter by S - and SS -waveform data.

Crust

Our preferred velocity model is given in Table 2 with a 3.75 km surface layer of 2.55 km s^{-1} (same as that of Chen

& Molnar 1981), followed by 16.25 km of 3.5 km s^{-1} , 20 km of 3.7 km s^{-1} , and 30 km of 3.8 km s^{-1} .

The source-station paths used in this Love wave investigation are given in Fig. 6, along with two P_{nl} paths discussed later. It is difficult to measure the initial arrival time of Love waves, so the first large pulse was used to denote relative timing and the synthetic has been aligned accordingly. Fig. 6 indicates the number of seconds the synthetic is faster than the observed for that particular ray path. The comparison of the data and synthetics is given in Figs 7 and 8.

Table 2. Velocity models for the Tibetan Plateau (TIP) and eastern China (ECH).

Depth (km)	TIP (km/sec)	ECH (km/sec)	Depth (km)	TIP (km/sec)	ECH (km/sec)	Depth (km)	TIP (km/sec)	ECH (km/sec)
0	2.550	3.450	150	4.550	4.440	290	4.705	4.668
3.75	3.500	3.450	160	4.550	4.467	300	4.708	4.675
10	3.500	3.700	170	4.590	4.484	310	4.712	4.682
20	3.700	3.800	180	4.625	4.501	320	4.715	4.695
30	3.700	3.850	190	4.658	4.518	330	4.718	4.710
35	3.700	4.650	200	4.668	4.535	340	4.721	4.720
40	3.800	4.650	210	4.675	4.552	350	4.725	4.730
70	4.600	4.600	220	4.680	4.569	360	4.730	4.740
80	4.600	4.550	230	4.685	4.586	370	4.740	4.750
90	4.600	4.500	240	4.690	4.603	380	4.750	4.760
100	4.600	4.450	250	4.690	4.620	390	4.760	4.770
110	4.600	4.400	260	4.693	4.637	400	4.770	4.770
130	4.550	4.400	270	4.697	4.654	405	5.014	5.014
140	4.550	4.420	280	4.701	4.660	425	5.050	5.050

In Fig. 7, we display the data whose source mechanisms are known (Holt & Wallace 1990), along with the synthetics of proposed models, where TIP indicates the synthetics appropriate for the model developed in this study, CHEN associated with model S7 of Chen & Molnar (1981), and CHUN computed from the model derived by Chun & McEvelly (1985). The data and synthetics are displayed in absolute traveltimes. From this figure, the waveform matches of TIP are better than the others, and the traveltimes at stations NDI and SHL are better. However, for the paths of event 24 to NIL, and event 13 to LAH, the traveltimes of TIP are 13 s faster than the data and are not as good as CHEN. CHUN is slow. In Fig. 8, the time shift was applied for each comparison. In this figure, the depth used to generate the synthetic is given. The depths may be different

from the corresponding ones given in Table 1. Because the source depth is poorly known, we just compared the data of unknown source depth with the data of known source depth to estimate the source depth. The basic assumption is that the source depth should be roughly the same if the two data are roughly alike. A strike-slip source with a time history (2, 2, 2) trapezoid was used to generate all synthetics. From these two figures, the traveltimes and the waveforms fit the data reasonably well, although TIP is faster, or slower for certain paths. We consider this model to be an average velocity distribution of the crust of the Tibetan Plateau which is considerably faster than previously proposed models.

Upper mantle

The upper mantle shear velocity distribution of the Tibetan Plateau beneath the crust is constrained by 11 *S*-waveforms with distances from 15.5° to 27.2°, and 16 *SS-S* waveforms with distances from 35.3° to 59.7°. Some of the *S*-wave data are from Lyon-Caen's paper (1986), and some of the *SS-S*-wave data are from Wang & Yao's (1989) paper. The traveltimes of the *S*-waves are not used, for they are rather scattered, and a large portion of their paths lie outside the Tibetan Plateau. Note that the *SS-S*-waveform data are controlled by triplication positions or differential times where rays share common paths near the source and receiver and thus are much less susceptible to traveltimes offsets caused by lateral variation (Grand & Helmberger 1984a). The ray paths of the *S*-wave data and the bounce-points of the *SS*-wave data are given in Fig. 9(a). The triangles represent the stations; stars represent the events generating the *S*-waves; circles represent the bounce-points of the *SS*-waves for distances greater than 45°; and squares represent the bounce-points of the *SS*-waves for distances less than 45°. In order to avoid the strong lateral heterogeneity, we did not use the *SS*-wave data with bounce-points near the boundary of the Tibetan Plateau.

The starting model for the upper mantle shear velocity structure of the Tibetan Plateau is TNA (Tectonic North America, Grand & Helmberger 1984a), with the crustal model derived above. After comparisons of synthetics and the data for several dozens of models, following a trial-and-error procedure, we obtained model TIP; see Fig. 5 and Table 2. This model has a 60 km thick lid of 4.6 km s⁻¹, and 40 km of 4.55 km s⁻¹ below. It does not have a distinct low-velocity zone, and is shield-like below.

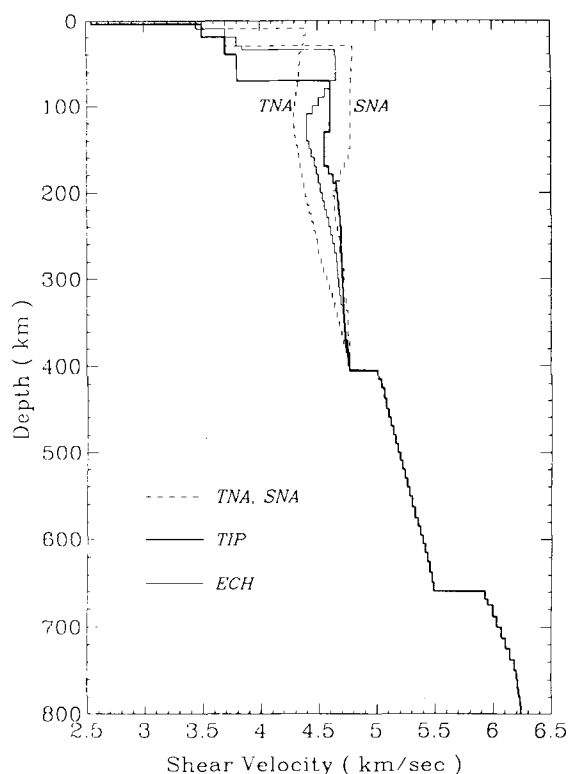


Figure 5. Shear velocity models TIP (Tibetan Plateau) and ECH (southeastern part of China) derived in this study compared to profiles of the Canadian shield (SNA) and tectonic western North America (TNA).

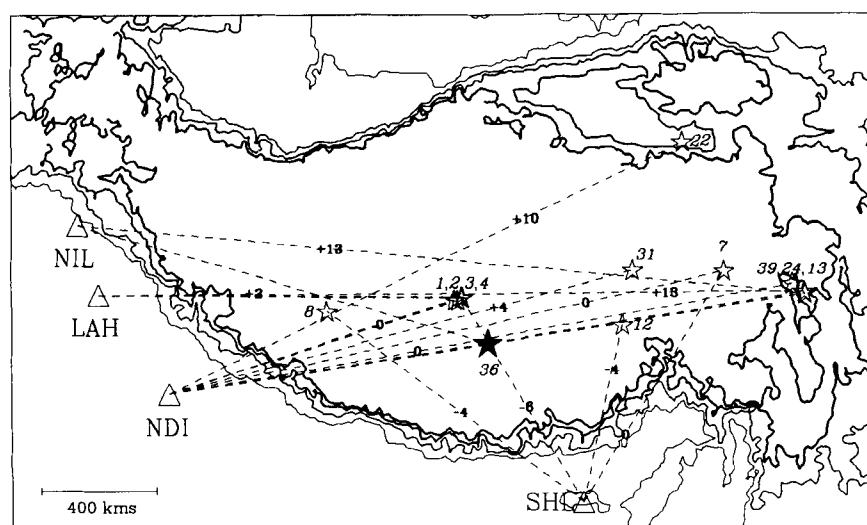


Figure 6. The ray paths of Love wave data used to derive the velocity distribution of the crust of the Tibetan Plateau, where the stars are sources, and the triangles are stations. The numbers are the differential maximum amplitude traveltimes of the data compared to the synthetics. The + sign means the model is faster in seconds. The number beside the source is event number of Table 1. The isobath relief contour lines with altitude of 1000, 2000, 3000 and 4000 m are given to define the physical boundary of the Tibetan Plateau. The dark star, event 36, is the location of the P_n -wave source.

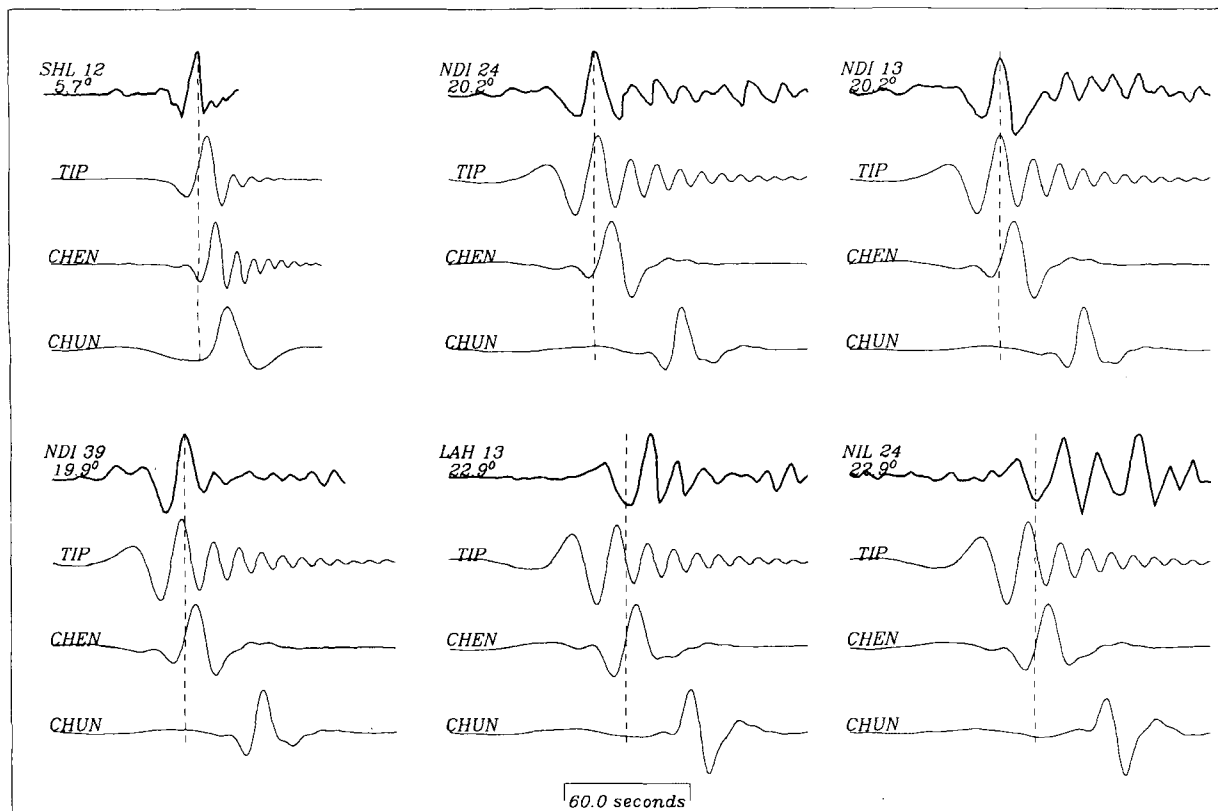


Figure 7. Synthetic comparison of different models with the data from known source parameters. In each group, the first trace is data with station name and event number in Table 1, along with the distance. The second, third and fourth traces are the synthetics of models TIP, CHEN, CHUN respectively.

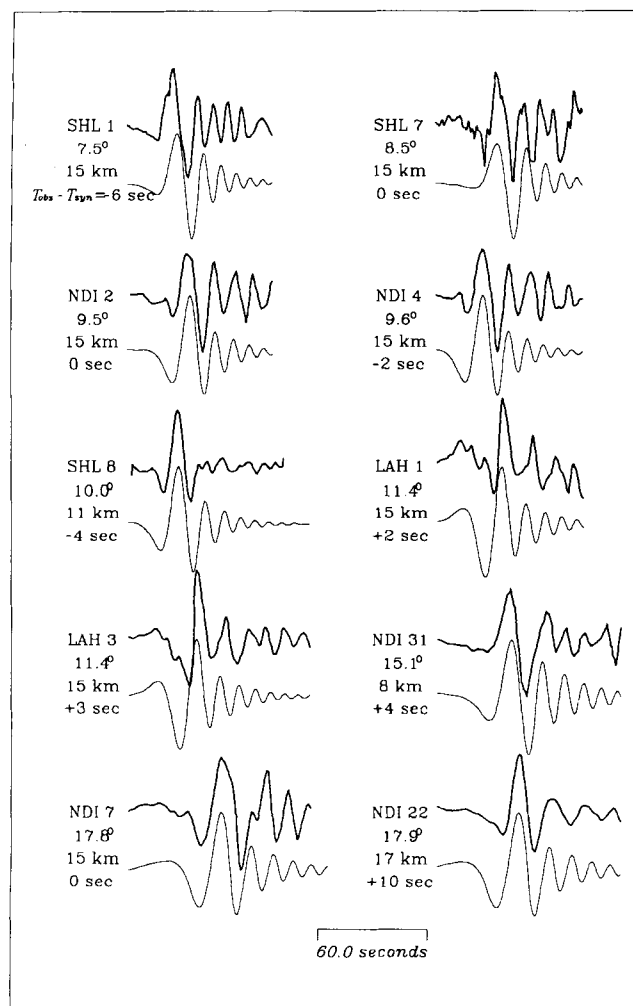


Figure 8. The Love wave data for paths shown in Fig. 6 compared with the synthetics. Upper traces are the data, the lower ones are synthetics when the amplitude are normalized, and shifted by the amounts indicated by $T_{obs} - T_{syn}$. On the left of each comparison are the station names and the event number given in Table 1 followed by the distance, source depth and $T_{obs} - T_{syn}$.

Figure 10 shows the comparison of the observed waveforms with synthetics. Because most of the *S*-wave data do not correspond to pure paths and sample an area with large heterogeneities, it is difficult to say which part of the data gives the most definitive information about the Tibetan Plateau. However, by comparing the paths indicated in Fig. 9(a) we see that the shallowest structure is sampled best by the western station, NIL. Almost all of the data and synthetics have three arrivals that are due to three sets of rays, one bottoming above the 405 km discontinuity (branch AB), one bottoming below the 405 km discontinuity and above the 670 km discontinuity (branches BC and CD), and another bottoming below the 670 km discontinuity (branches DE and EF). We will generally refer to branches by single letters, which will denote the two arrivals forming the cusp designated by the letter (Fig. 11). With long-period data the two geometric arrivals forming a branch usually cannot be distinguished. When there is possible confusion in the branch name, we will indicate a full designation. A good fit

of the waveforms and, therefore, differential traveltimes of branches A, B, C, D, E and F to the data at distances of 17.2°, 20.1°, 24.0°, 24.6°, 25.3°, and 26.7° is achieved. Note that the A branch is missing from the LZH data (18.4°) indicating a shallow heterogeneity along the path (Grand & Helmberger 1985). The differential traveltime between the branches A and C of the data recorded at NIL at a distance of 15.5° is 3.5 s faster than that of the synthetics, and that of the data also recorded at NIL at a distance of 16.4° is 2 s faster than that of synthetics. Perhaps these differences were caused by the local faster structure and thinner crust thickness near the station NIL. The amplitude of the E branch for QUE data at a distance of 21.0° could be due to the missing A branch.

The traveltimes and waveforms of *S*-waves alone do not yield definitive constraints on the velocity distribution of the Tibetan Plateau, because large parts of the ray paths are outside the region. Fig. 12 shows the *SS*-*S*-wave data with synthetics of the model TIP. The fits of the waveforms and differential traveltimes between the first and the second arrivals (F and D branch), and the *S*-wave of the data recorded at SEO at a distance of 54.5° with the synthetics indicate that the shear velocity distribution beneath the 405 km discontinuity is the same as that beneath the Canadian Shield (Grand & Helmberger 1984a, b). The source functions used for the synthetics of *SS*-waveforms are the teleseismic *S*-waveforms. The advantage of using the teleseismic *S*-waveform as a source function is that the importance of the source mechanisms and source depth is almost completely eliminated. The waveforms of *S*-waves are the sum of direct *S*- and *sS*-waves. The traveltime difference between these two phases is controlled by the source depth and the ray parameter, or take-off angle. The amplitude ratio is determined by the source mechanism (Langston & Helmberger 1975). The different *S*-waveforms at different distances are due to the ray parameters. The ray parameter changes very slowly with distance beyond 15°, becoming nearly a constant for distances beyond 25°. Thus the effects of source depth and source mechanism are almost the same on triplication *SS*-waves as on teleseismic *S*-waves.

The differential traveltime of the C branch and *S*-wave of the data recorded at MSH at a distance of 35.3° is about 5 s faster than that of the synthetics, and the branch A is absent. The bounce-point for it is the far west point indicated in Fig. 9(a). The ray of the C branch in this case travels almost entirely in the upper 405 km with only a very small part of it going below the 405 km discontinuity. A large part of the time difference is due to the more than 10° of horizontal travel distance in a shield-like region (Rial *et al.* 1984) outside the Tibetan Plateau. Also, the lateral heterogeneity could cause some difference in the differential traveltime of *SS*- and *S*-waves. The differential traveltimes and waveforms of *SS*- and *S*-waves of the HKC (35.7°) data, see Fig. 12, are matched very nicely for the branches C and E, although the A branch is not clear. The beginning waveform of the HKC station at a distance of 52.0° is most likely *S*. If it is a combination of *S* and *sS*, the source depth should be about 80 km, and the amplitude of the second one would not be likely to be so large. If we use all of the beginning waveform as the *S*-wave, or source function, the synthetics for the *SS*-wave are very good, but we could not label the branches. The waveforms of the *SS*-waves of HKC

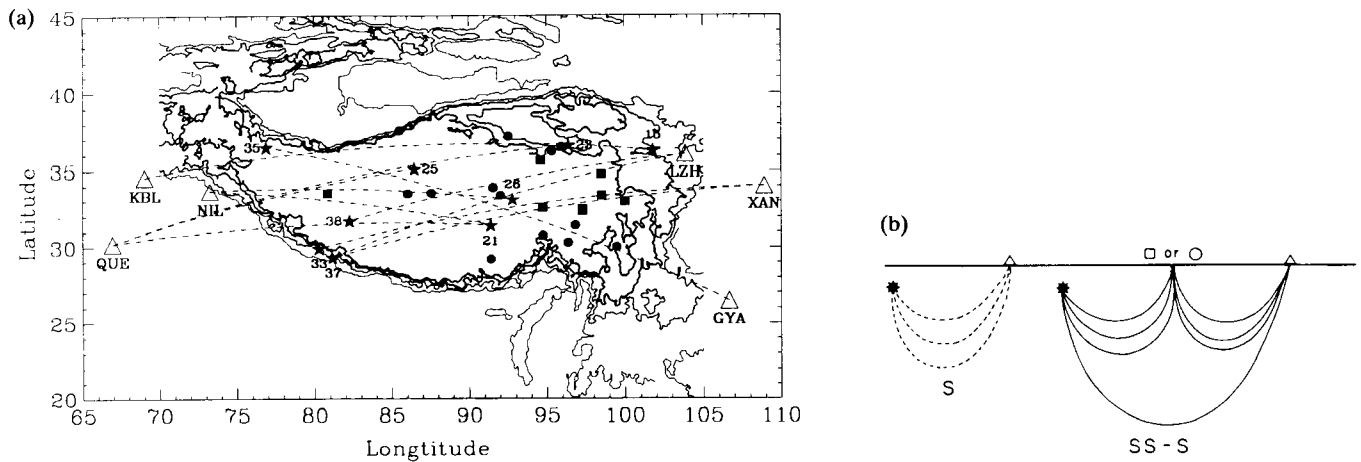


Figure 9. (a) The ray paths, dotted lines, of *S*-wave data, and the bounce-points of the *SS*-wave data used to study the upper mantle shear velocity structure of the Tibetan Plateau. Circles represent the source–receiver distances greater than 45° , squares less than 45° , stars are sources, and triangles are stations. The solid lines from thin to thick are contour lines with 1000 m, thinnest, 2000, 3000 and 4000 m, thickest, above sea level. The number beside the source is event number in Table 1. (b) Schematic illustration of rays producing *S*-waveforms (left), and *SS*-waveforms (right).

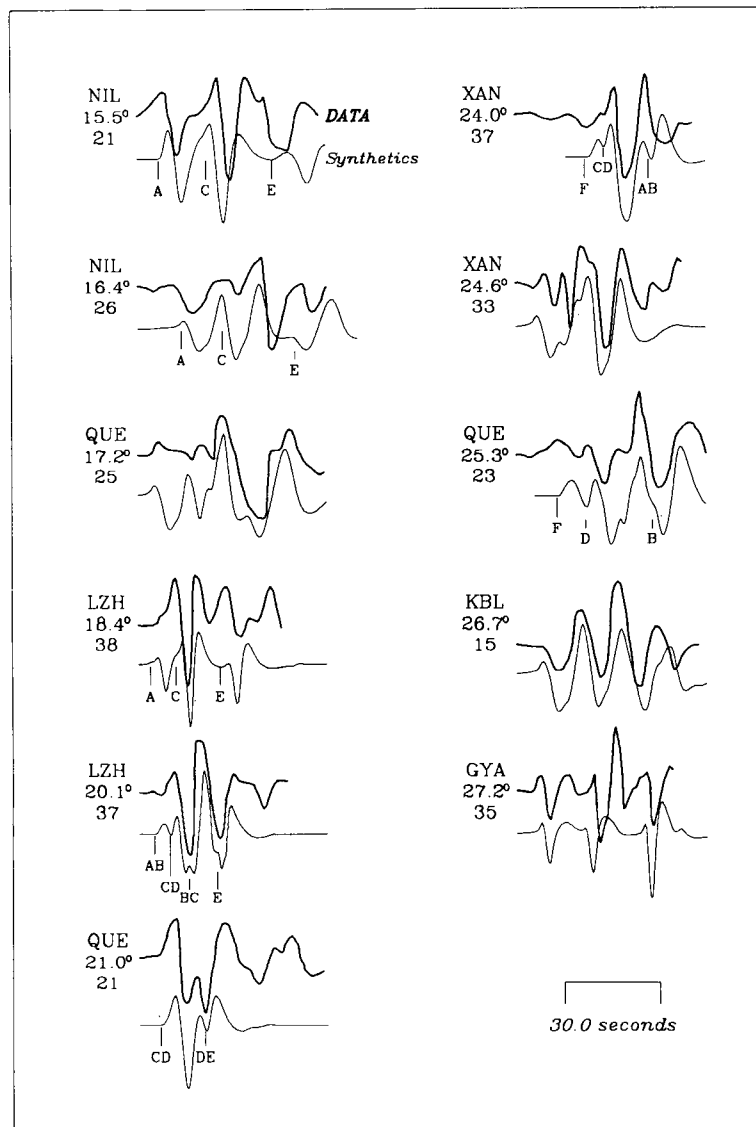


Figure 10. The comparisons of the waveforms of the *S*-waves for the paths of the Tibetan Plateau with the synthetics using the model TIP. 'A', 'B', 'C', 'D', 'E' and 'F' are the branch names of the corresponding arrivals (Fig. 11). On the left of each data–synthetic comparison are station names, distances and event number.

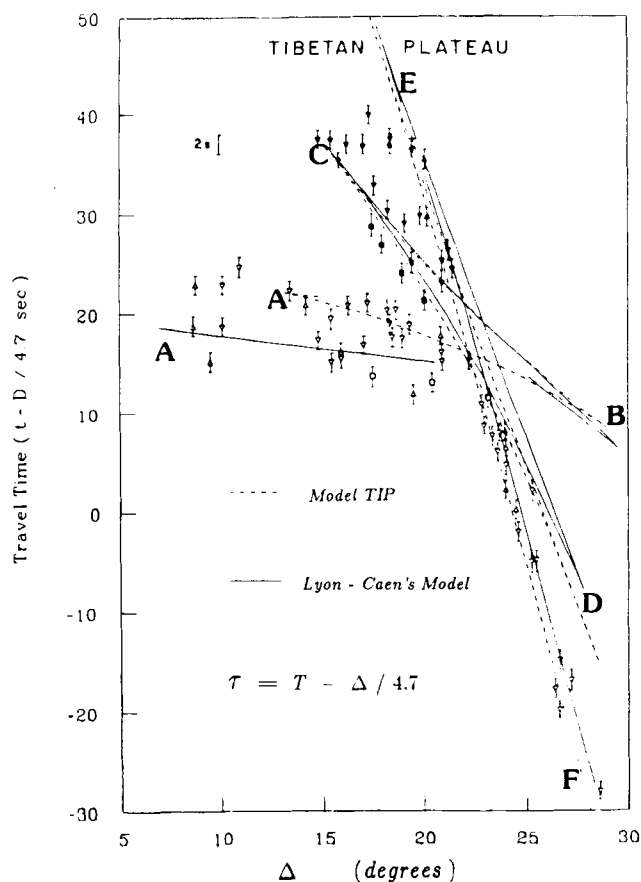


Figure 11. Triplication curves of the model TIP and Lyon-Caen's model, and Lyon-Caen's traveltime data of *S*-waves for the Tibetan Plateau paths. The different symbols indicate the properties of the path (Lyon-Caen 1986, Fig. 8).

at a distance of 51.0° do not agree well with that of the synthetics, but the match of the differential traveltime is not bad. The arrival between the *S*- and *SS*-waves on the data HKC 51.0°, GZH 51.8°, HKC 52.0°, SEO 54.5°, and HKC 59.7° is the phase *ScS*.

The synthetic fits to this data set proved particularly difficult. The reason is in the inherent complexity of the structure itself in terms of heterogeneity. Nevertheless, it appears that the derived model for the structure beneath the Tibetan Plateau fits the *S*-*SS* waveform data better than existing models, as will be discussed in more detail later.

Eastern China

The data coverage of the eastern portion of China is presently lacking but will become more complete when the new digital array becomes operational. The ray paths of the data used for the study of eastern China are displayed in Fig. 13. It is clear from the figure that the region sampled includes the Yangtze Craton and the southern half of the Sino-Korea Craton. Although the region is relatively complex, we will assume a uniform upper mantle structure as a first-order approximation of the area. The data set we used to constrain the upper mantle shear velocity distribution includes five *S*-wave data, distances from 19.0° to 24.5°, and 10 *SS*-wave data, distances from 33.2° to 39.7°.

The model, ECH, we obtained, is given in Table 2 and Fig. 5. The comparisons of the synthetics with the data are given in Figs 14 and 15.

In Fig. 14, we display synthetic and *S*-wave observation comparisons along with the theoretical responses and source function estimates. The branches are identified on the theoretical responses similar to Fig. 10 discussed earlier. Although all the branches cross each other in this distance range, we can see pulses of branches on both the data and the synthetics. The traveltime of the synthetics is 3 s faster than that observed at HKC (19.0°), 3 s slower than that of ANP (20.8°), 4 s slower than that of SHL (22.9°), 7 s slower than that of SEO (23.2°), and 9 s slower than that of ANP (24.5°) (Fig. 13). The fit of the traveltimes is certainly reasonable for such a large laterally heterogeneous area. The synthetics are produced by convolving the theoretical responses (Earth responses) with the effective source functions which contain *sS*. The source function of ANP (20.8°) is the *S*-waveform observed at MAT (36.0°, Fig. 15). The other source functions are theoretical predictions assuming a strike-slip at SHL and SEO, and a dip-slip at ANP and HKC. The bottom two observations at SEO and ANP, showing the interference of F and D branches, are very similar to those displayed in Fig. 17 of Grand & Helmberger (1984a).

Figure 15 gives the comparisons of the synthetics of *SS*-waveforms and the data. The *SS*-waveform recorded at a distance less than 45° gives not only information about the bounce-point, but also information about a large part of the upper mantle structure along the ray path. All of the *SS*-wave data we have used are less than 40°, so this may cause some difficulties for the large lateral heterogeneity. Also it is difficult to locate the E, F branches of the model. The complexity of the waveforms of SHK (35.0°) is due to the depth of the source, 134 km. We have not matched *sS*- and *sSS*-waves, so the synthetic is incomplete. Note that seven of the 10 seismograms used are recorded at MAT, and one third of their ray paths lie out of continental China (Fig. 13). Actually, for some of the *SS*-wave data, only one third of their paths and bounce-points are in the eastern part of China, Yangtze Craton, and the south half of the Sino-Korea Craton. It can be inferred from the data and the synthetics (Figs 14 and 15) and the traveltime residuals (Fig. 13) that the velocity of the Sino-Korea Craton is faster than that of the Yangtze Craton, and that the northern part of Yangtze Craton is faster than the southern part. The model we derived here is, obviously, only a very approximate model for the upper mantle shear velocity distribution for the eastern part of China. Nevertheless, these preliminary results suggest that the mantle beneath eastern China is predominantly shield at depths greater than a few hundred kilometres. The large traveltime offsets suggest strong shallow lateral variation. More data will be required to resolve the connection with the surface geology and interplate interaction.

DISCUSSION AND CONCLUSIONS

In this section we will briefly compare synthetics associated with existing models (Fig. 16) proposed for the Tibetan Plateau with some of the key *SS*-*S* observations. The *SS*-*S* data are the least contaminated by lateral variation as

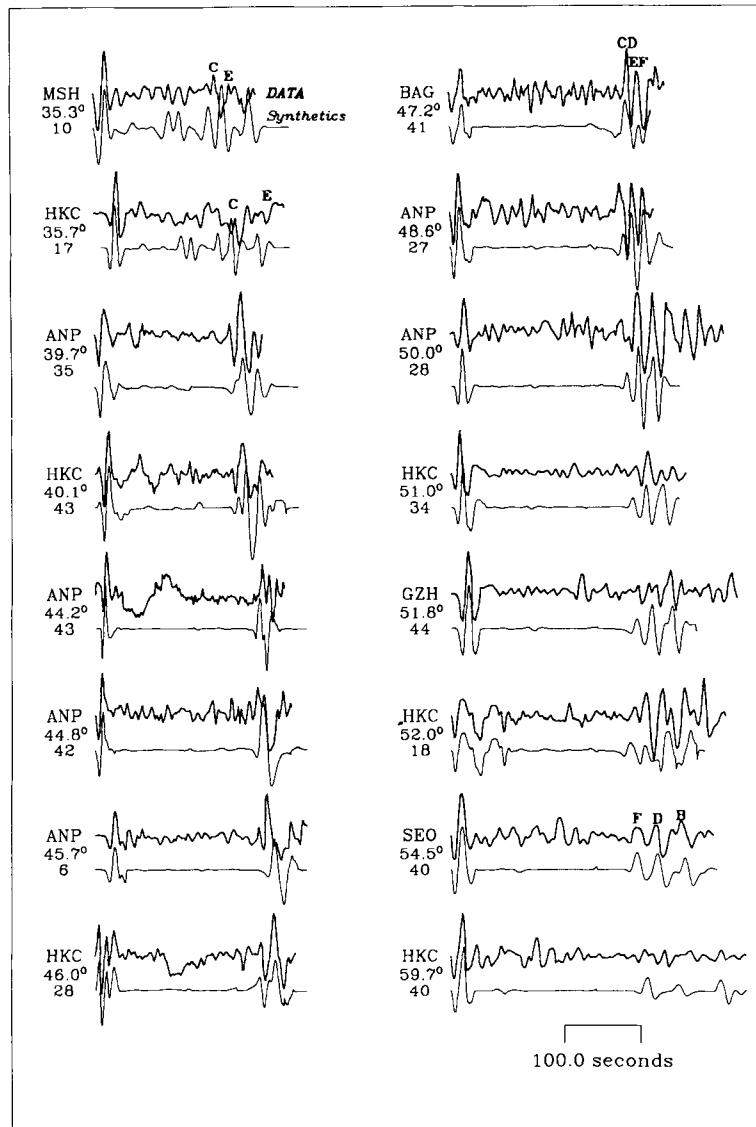


Figure 12. SS- and S-wave data for the paths with mid-points in the Tibetan Plateau and the synthetics of the model TIP. The S-waves are aligned with synthetic S-waves. The observed S-waveforms are used as the source function. On the left of each data-synthetic comparison are station names, distances and event number.

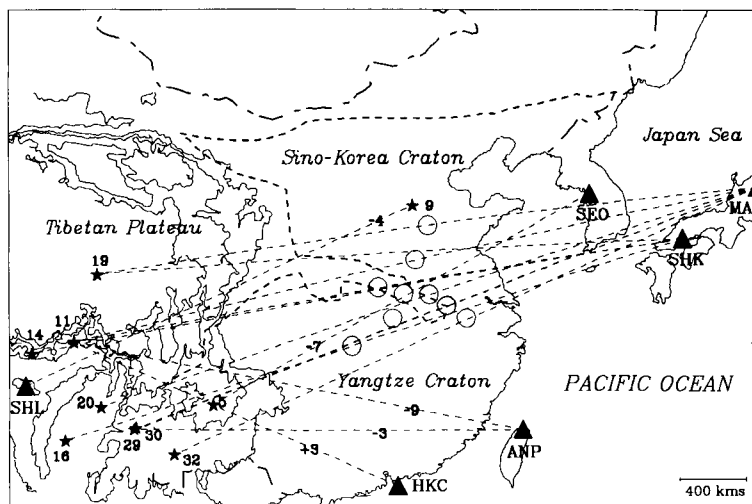


Figure 13. The ray paths of the S- and SS-wave data used to derive the upper mantle shear structure of the southeastern part of China. The stars are sources, and the triangles are stations. Circles indicate the mid-points of the SS data. Numbers near stars are event numbers, as in Table 1. Numbers with '+' or '-' sign on the rays of S-waves are the differential traveltimes of the data relative to the synthetics using the model ECH. The symbol + means that the model is faster than the data.

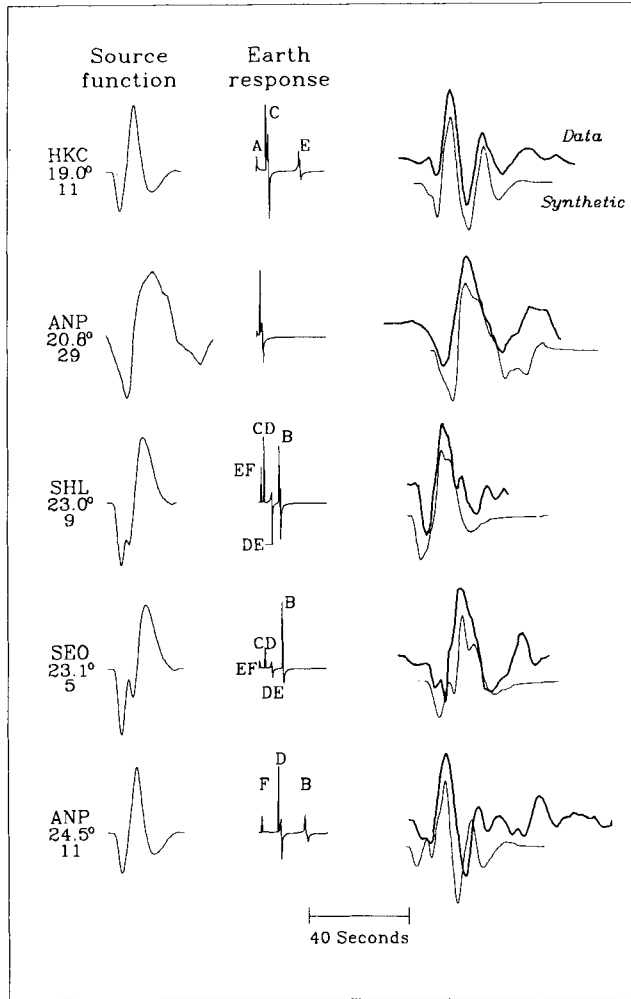


Figure 14. *S* data for the paths of southeastern China and the synthetics using the model ECH. Numbers below the distances are event numbers as displayed in Table 1. They are lined up with maximum amplitudes.

discussed earlier and thus the most definitive. This will be followed by an in-depth discussion of the upper 200 km of the models since this is the region where models differ the most and are the most significant in terms of tectonic implications. The waveforms of *SS-S* waves are the results of the interference of the five branches AB, BC, CD, DE and EF (Fig. 11). Since the traveltime branches are nearly straight lines, we can get a shear velocity model for a homogeneous structure if we have two ideal waveforms of *SS-S* waves at a distance near 30°–60°. We present three key data taken from Fig. 12, located at roughly 10° intervals, namely, HKC at 35.7°, ANP at 44.8°, and SEO at 54.5° in Fig. 17. The waveforms of SEO at 54.5° are particularly meaningful, because waveforms of the different branches have separated. At ANP the branches are all together. In order to see clearly the differences between the data and synthetics, we have inserted the vertical lines. The bottom four traces of each group are synthetics for proposed models for this region.

Comparing the various models presented in Fig. 16 we note that TIP has a faster crust and a slower lid than the

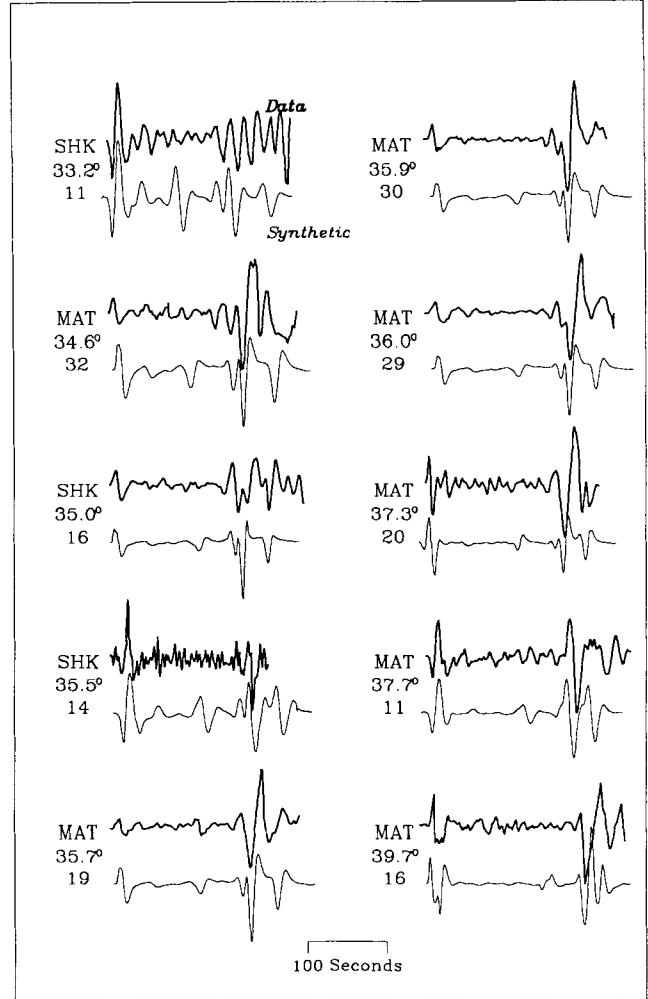


Figure 15. *SS* and *S* data for the paths with mid-points in southeastern China, and the synthetics using the model ECH. The *S*-waves are aligned with synthetic *S*-waves.

other models. Thus, the S_n and P_n arrival time predictions for TIP are distinctly slower than others. Comparing with the data at HKC (35.7°), the branches C and E of the TIP synthetics are about 2 s faster than the data; this means that either the shear velocity of the upper part, especially the crust, is faster than the observed or the crustal thickness at the bounce-point is greater than the model TIP, as discussed earlier. The C branch, and the E branch of the synthetics of Lyon-Caen's models (Ltib) are 7.5 and 4.5 s slower than that of the HKC data. The synthetics for Wang's model are also slower than the HKC data by a few seconds. The branches arrive at almost same time for the ANP (44.8°) data. The synthetics of Wang and Ltib are slower. The F, D and B branches of Ltib are 3.5, 5 and 16 s slower than those of the SEO data respectively. The B branch of Wang is 11 s slower than that of the SEO data. Lyon-Caen's Indian model presents a comparison of Indian Shield with the Tibetan Plateau. The slow B branch of Ltib and Wang suggest that the velocities of the upper 200 km of the models are too slow.

Records at this range are particularly important in fixing

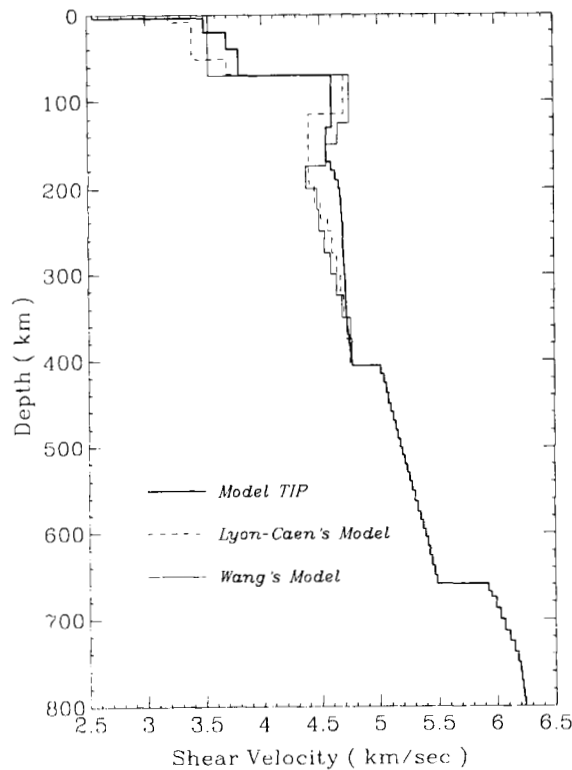


Figure 16. Comparison of the existing models for the Tibetan Plateau.

the shallow mantle velocity. A few additional SRO records were found sampling this range as displayed in Fig. 18. The waveform fits are not good, probably indicating the heterogeneity of the region, but the timing on the B branch relative to the other triplications is indicative of shield structure. This suggests that the upper mantle in this region is, indeed, fast.

To check our results further requires some absolute traveltimes constraints or better knowledge about the earthquake sources used in terms of location and mechanism. For instance, we used the ISC location and origin time for event 22 in timing NDI, see Fig. 6, and found a residual of +10 s. This means that the model TIP is 1.5 per cent faster than the average velocity along this path, but if we used the USGS location and origin time for this event, the traveltime residual would be +2 s, which means this model is very good. We have no particular reason to say the ISC location and origin time are better. We choose to use them simply for book-keeping. Since these locations given by the agencies do not use depth phases in their analysis we decided to do an indepth study of one of these events to assess uncertainties and establish a few absolute traveltime constraints. Event 36 was selected for this purpose since it also has a few P_{nt} -waves on scale. The origin time and location used are 3:2:47.2, 30.506°N, 88.583°E, and an epicentral depth of 33 km was assigned by NEIS. This event is big enough to be recorded worldwide, $m_b = 5.7$, $M_s = 6.2$.

First, we derive the source depth by modelling the teleseismic P waveforms. The results are given in Fig. 19 where the best fitting source depth is 10 km. We estimate the errors in depth to be less than 3 km, and fault plane less

than 5°. Fig. 19 displays the best overall fit of different runs, indicating a strike of 160°, a dip of 60°, and a rake of 250°. Stations POO and CHG are within upper mantle distances and the P -waveforms recorded by them are complicated by triplications, and matched well by the synthetics. The model used in these calculations was derived by comparing TIP with a P -wave model for the Canadian Shield, namely S25 (LeFevre & Helmberger 1989) and SNA (Grand & Helmberger 1984a), and using the relationship with shear velocities of rocks of basaltic composition (Ludwig, Nafe & Drake 1970) (Table 3). Some bad-looking seismograms are due to digitizing since the line-thickness of the recordings is 3–5 s thick, and the maximum amplitudes of some recordings do not exceed half of the line-thickness, such as MUN.

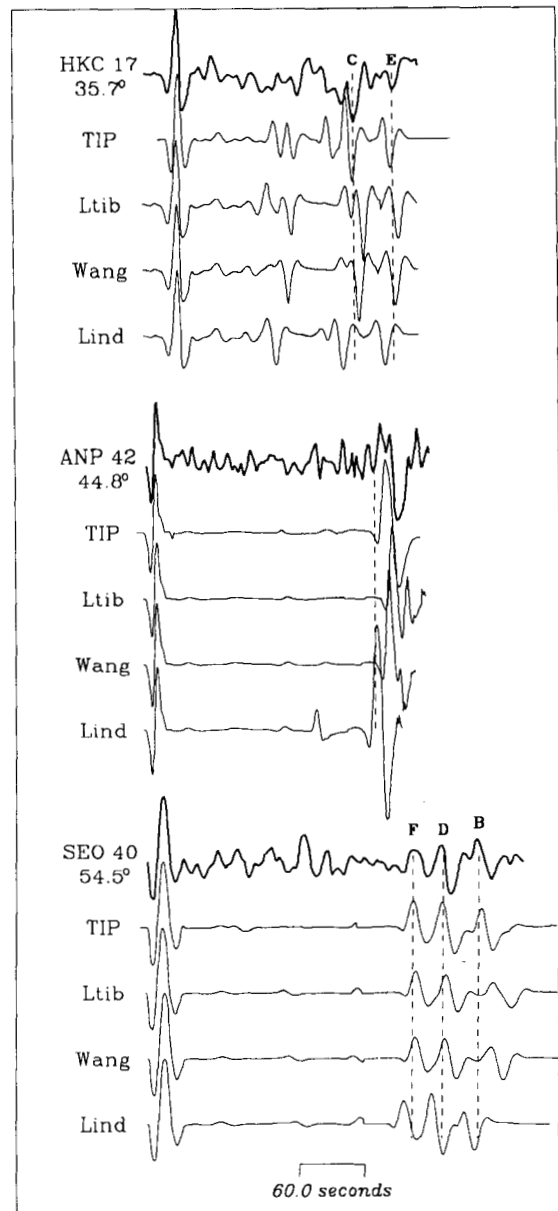


Figure 17. Comparison of the data and synthetics of models TIP, Ltib, Lind, and Wang's model. Ltib is Lyon-Caen's model for the Tibetan Plateau, Lind is Lyon-Caen's model for the Indian shield. Letters on top of the data are the branch names (Fig. 10).

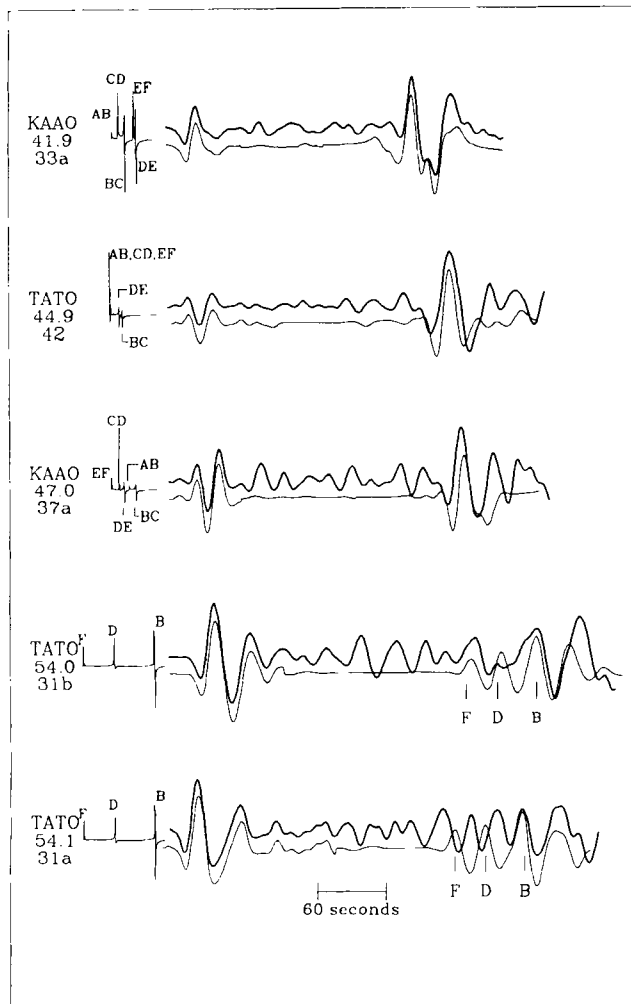


Figure 18. Comparison of the data recorded by SRO stations (upper traces) and synthetics (lower traces) from model TIP. On the left are the stations, distances, and event numbers. On the right of the stations are the Earth responses, on which the branch names indicated.

The results of the relocation, based on the new source depth, are given in Table 4. In this table, STAT are station names; TPK are the times we picked from vertical component of short-period WWSSN data after minute mark in second; TPKP are the times picked by station operator; TOBS1 and TOBS2 are the observed P -wave traveltimes after the old and new origin times; TCOM1 and TCOM2 are the computed P -wave traveltimes for the old epicentre and origin time, and for the new epicentre and origin time. DT1 and DT2 are the residual traveltimes after Dziewonski & Anderson's (1983) station correction; the minus sign means TCOM is faster than TOBS. The standard deviation is 1.5 s. This error mainly comes from the contributions of the three stations UME, HLW and STU, whose deviations are greater than 4 s. After relocation, the location becomes 30.658°N , 88.649°E , and the origin time becomes 03:02:43.7. The new location is 18 km from the location given by NEIS. The origin time is 3.5 s earlier than that given by NEIS, 1.3 s earlier than that given by ISC. We used the modified P -wave TIP model as discussed before for the source region

and JB for the receivers to calculate the TCOM. For a distance greater than 30° , the half way traveltime difference between the model TIP and the model JB is only 0.5 s. If we used the JB model for the source region, the new location would be 30.625°N , 88.632°E , only 4 km from the location given by different source velocity models and origin time would be 03:02:43.7, only 0.04 s difference. This is because the upper 400 km of JB model is slow, or the average velocity of the upper 400 km of JB is about the same as that of the model TIP.

As a check on the accuracy of our crustal model, we make synthetics of P_n -waveforms and compare them with the data recorded at the stations NDI and NIL due to the Tibetan earthquake we relocated above. Fig. 20 displays the P_n data along with the synthetics of the model TIP. The method used to make these synthetics is reflectivity (Mallick & Frazer 1988). The synthetics of NDI is shifted left 1.5 s and that of NIL is shifted 0.5 s. We present only three seismograms here since the amplitudes of the north components of both stations are very small and the vertical component of the NIL station was not available. We can see from Fig. 20 that the fits are good. This means that the average velocity structure and the crustal thickness of the Tibetan Plateau can be approximated by the model TIP for the paths (Fig. 6), although these paths only sample the southern part of the Plateau. The time shifts given above are largely caused by the dipping Moho. Thinning the crust at the receiver by 20 km reduces the P_n traveltime by 2.2 s; see Fig. 6. Thus, considering the possible crustal thickness beneath the stations, and assuming that the crustal thickness beneath NDI and NIL is 50 km, we conclude that the model TIP is about 0.7 s faster for the path to NDI and 1.7 s faster for that to NIL. This implies that the P -wave velocity of the mantle for these paths is 8.23 km s^{-1} instead of the 8.29 km s^{-1} that we used in the above flat-layered P_n calculation.

Barazangi & Ni (1982), and Ni & Barazangi (1983) used P_n - and S_n -waves crossing the Tibetan Plateau, and obtained velocities of 8.42 km s^{-1} for P_n , and 4.73 km s^{-1} for S_n . They concluded that these velocities were very similar to those beneath the Himalaya Mountains and the Indian shield, and suggested that the Indian continental lithosphere underthrusts the Tibetan Plateau at a shallow angle. However, our earlier experiments suggest a high-velocity bias for most recording geometries if only simply assuming a flat-layered model. For instance, in Fig. 4, the S_n arrives about 3.5 s earlier in the model d than a flat structure with a crustal thickness 70 km, model f. A mantle velocity would be 4.69 km s^{-1} , instead of 4.6 km s^{-1} used in Fig. 4. Thus, an average S_n velocity of 0.1 km s^{-1} greater than the average velocity beneath the Tibetan Plateau is very likely obtained if only S_n data are used. Seismograms for 2-D models crossing this interesting region will be discussed in a later paper.

Our results (TIP) are consistent with that of the attenuation study of pure path long-period Rayleigh waves across the Tibetan Plateau by Romanowicz (1984). The conclusion of 'no lid' for the Tibetan Plateau is consistent with that for the central Chang-Thing of Tibet from pure path phase velocity measurement of long-period Rayleigh waves by Brandon & Romanowicz (1986). These results are similar to those obtained from modelling multibounce

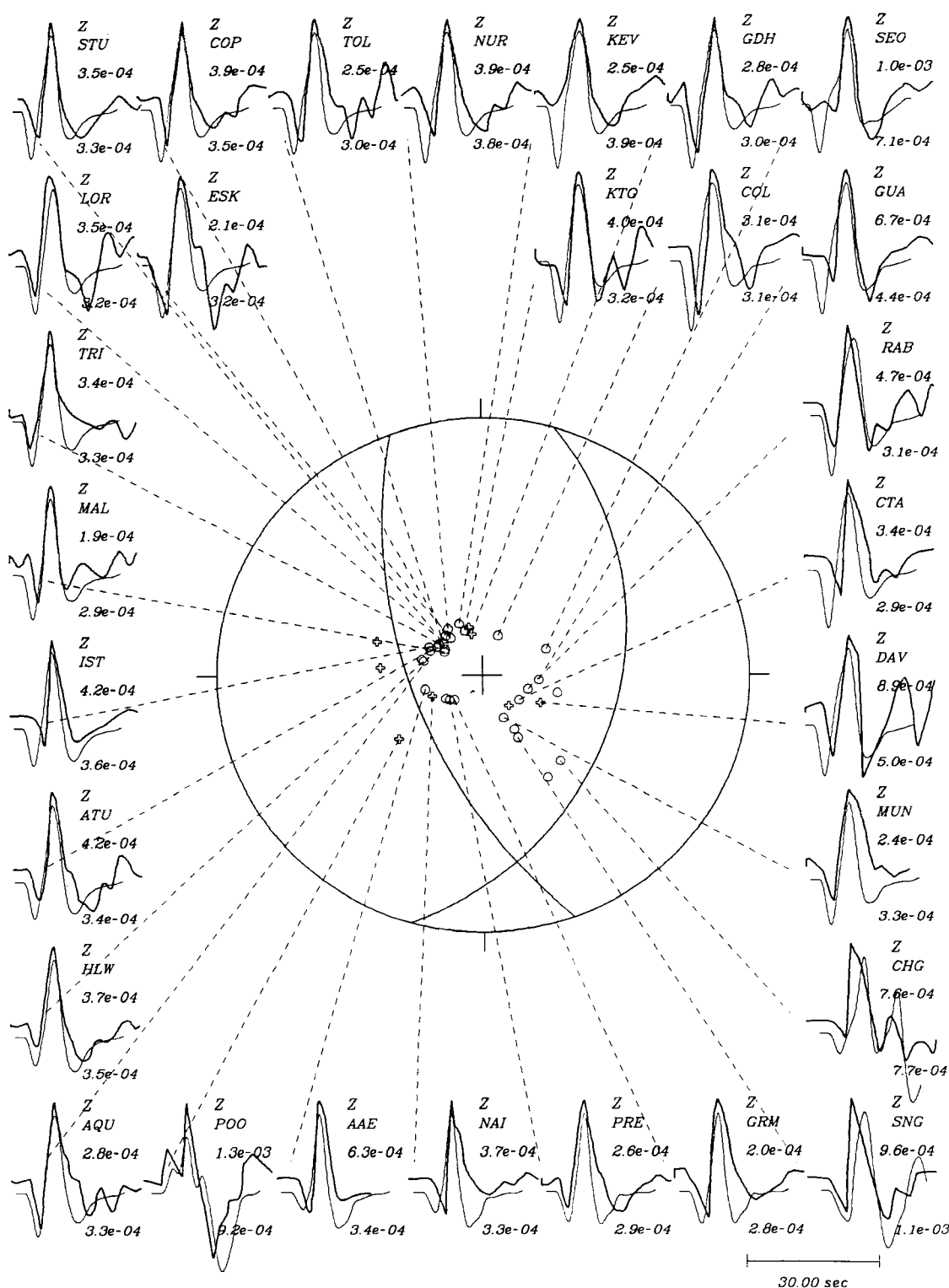


Figure 19. Source mechanisms, and synthetic comparison with the long period *P*-wave WWSSN data of the 1980 February 22 Tibetan earthquake. The origin time is 3:2:43.7, epicentre location is 30.658° N 88.649° E, source depth is 10 km. The strike, dip and rake are 160°, 60° and 250° respectively. the moment is 8.0×10^{24} dyne cm and the source function is a trapezoid (1, 1, 1). The darker traces are the data, and the lighter ones are synthetics. On the right of each data-synthetic comparison are the component of the data used ('Z', vertical component), station name, the peak amplitude of the data, and the peak amplitude of the synthetics in centimetres using the moment given earlier. The (+) symbol indicates compressional, and little circles indicate dilational. If the polarity of the short-period data is different from that of its corresponding long-period data, we use that of the short-period data.

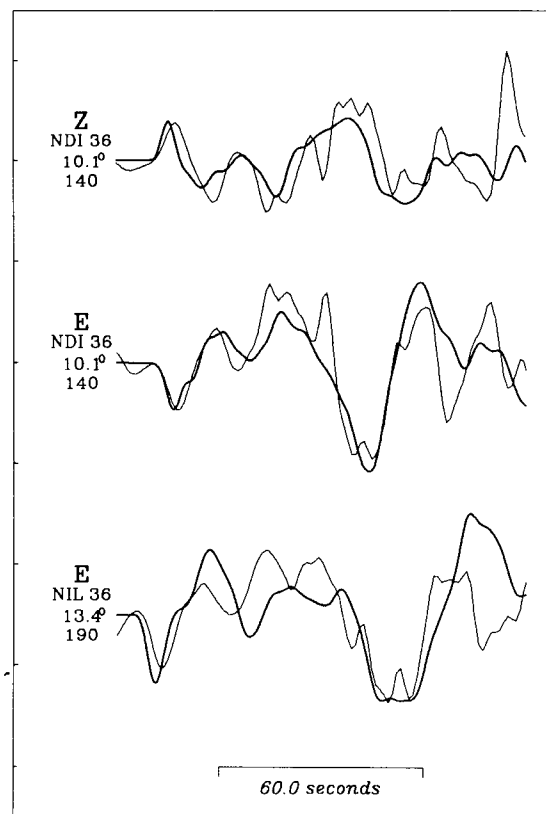
Table 3. Compressional velocities of TIP.

Depth (km)	Thick (km)	Vel (km/sec)	Depth (km)	Thick (km)	Vel (km/sec)
0.00	0.00	4.530	280.0	10.0	8.470
3.75	3.75	4.530	290.0	10.0	8.480
20.0	16.25	6.160	300.0	10.0	8.486
40.0	20.0	6.550	310.0	10.0	8.510
70.0	30.0	6.740	320.0	10.0	8.540
130.0	60.0	8.290	330.0	10.0	8.560
170.0	20.0	8.200	340.0	10.0	8.570
180.0	10.0	8.270	350.0	10.0	8.594
190.0	10.0	8.340	360.0	10.0	8.623
200.0	10.0	8.400	370.0	10.0	8.653
210.0	10.0	8.420	380.0	10.0	8.691
220.0	10.0	8.430	390.0	10.0	8.730
230.0	10.0	8.440	400.0	10.0	8.770
240.0	10.0	8.450	405.0	5.0	8.810
260.0	20.0	8.460			9.280
270.0	10.0	8.462			

S-waves by Grand & Helmberger (1985), who constructed a 2-D cross-section from Tibet to Europe. Resolution from their study begins at the edge of Tibet and indicates that the structure beneath the Tarim basin is similar to our results for Tibet, namely, a shield-like model with a slow upper 200 km. We do not presently have a detailed shear velocity model available for the eastern part of China, except that it appears similar to other shields. Thus, from this study, and the studies by Grand & Helmberger (1985), and Rial *et al.* (1984) we suggest that the upper mantle of the Eurasian plate is shield-like below 200 km.

Table 4. Relocation of 1980 February 22 Tibet earthquake. The location is 30.506°N, 88.583°E, and the origin time 03:02:47.2. After relocation: the location is 30.658°N, 88.649°E, and the origin time 03:02:43.7.

STAT	TPK	TPKP	TOBS1	TOBS2	TCOM1	TCOM2	DT1	DT2
AAE	51.3	50.0	544.1	547.6	544.8	545.5	-3.1	-0.3
ADE	57.8	59.3	730.6	734.1	733.4	733.8	-2.9	0.2
AQU	51.3	51.3	604.1	607.6	607.0	607.7	-4.7	-1.0
BAG	17.4	16.1	390.2	393.7	392.3	392.2	-2.7	0.9
BUL	36.1	36.0	708.9	712.4	712.3	713.0	-2.8	-0.0
CHG	14.8	14.9	207.6	211.1	212.3	213.4	-4.0	-1.5
COL	27.9	28.3	700.7	704.2	705.5	704.6	-5.1	-0.6
COP	37.1	37.8	589.9	593.4	594.1	593.5	-5.1	-1.0
CTA	26.1	26.0	698.8	702.3	702.7	702.9	-3.9	-0.6
DAV	36.4	34	469.2	472.7	471.3	471.5	-3.5	-0.1
ESK	34.7	34.8	647.5	651.0	652.1	651.5	-4.9	-0.9
GDH	36.6	36.3	709.4	712.9	713.5	712.7	-4.0	0.3
GRM	28.6		761.4	764.9	764.0	764.7	-3.5	-0.6
HKC	2.8	5	315.6	319.1	319.0	318.8	-4.9	-1.2
HLW	37.9	34	530.7	534.2	529.3	529.4	1.5	4.8
IST	29.4	25	522.2	525.7	526.4	526.2	-4.7	-1.0
JER	6.2		499.0	502.5	500.3	500.4	-2.2	1.3
KBL	40.8	41.1	233.6	237.1	237.9	238.0	-4.2	-0.7
KEV	54.9	55.0	547.7	551.2	551.4	551.2	-4.0	0.4
KTG	46.8	46.2	659.6	663.1	662.0	663.1	-3.6	0.7
LOR	24.3	25.1	637.1	640.6	642.3	640.6	-4.7	-0.8
MAT	32.0	31.3	464.8	468.3	468.8	467.9	-3.6	0.9
MUN	41.9	40	654.7	658.2	658.0	658.7	-2.5	0.3
NAI	43.9	44	506.7	509.2	509.0	509.8	-3.4	-0.6
NDI	11.6	11.5	144.4	147.9	146.6	147.6	-1.4	1.0
NIL	55.2		188.0	191.5	190.9	191.0	-2.8	0.5
NUR	48.8	49.5	541.6	545.1	546.0	545.3	-4.4	-0.2
POO	54.7	54.3	247.5	251.0	250.0	251.8	-2.2	-0.4
PMG	50.5	50	663.3	666.8	666.4	666.5	-3.3	0.1
QUE	2.8		255.6	259.1	259.5	260.1	-3.7	-0.8
RAB	57.4	57.5	670.2	673.7	672.3	672.3	-2.6	0.9
SHL	12.3	12	85.1	88.6	87.6	88.9	-1.3	0.8
SNG	17.6	19	330.4	333.9	333.1	334.1	-2.9	-0.4
STU	3.5	2.0	616.3	619.8	616.5	616.1	0.2	4.2
TOL	16.3	15.0	680.1	692.6	692.0	691.8	-3.5	0.3
TRI	43.0	42.9	595.8	599.3	600.9	600.5	-4.5	-0.7
UME	2.2	6.5	555.0	558.5	564.2	563.4	-8.9	-4.6

**Figure 20.** Synthetic comparison with P_{nr} -waveform data. The darker traces are the data, and the lighter ones are the synthetics. The starting times of the corresponding data and synthetics are 140 and 190 s. The data and synthetics are lined up with absolute time, with NDI synthetics shifted left 1.5 s, NIL synthetics shifted left 0.5 s. The numbers beside the station names are event numbers given in Table 1.

Although these results are preliminary in nature it would appear that the deformation of the European plate is confined mainly to the upper 200 km. This type of velocity distribution thus becomes an important piece of evidence to be used in deducing the tectonics of the area.

It is generally assumed that major underthrusting is occurring along the Himalayan arc as deduced from source mechanism studies; see Ni & Barazangi (1984) and others. The dynamic processes that lead to the formation and maintenance of a mean elevation of 5 km over some two million square kilometres behind the Himalayan arc appears more controversial. Essentially two hypothesis have been put forward, namely underthrusting and crustal shortening. Underthrusting in the NW Pacific results in complex crustal structures with a large low-velocity zone associated with the subducted upper crustal section; see Langston (1977). We did not find much evidence for such structures in this study. Crustal shortening has been suggested by Molnar and his associates. They argue that the temperature at the base of the crust is 250° to 300° higher than beneath platforms; see Chen & Molnar (1981). Increased radiogenic material per horizontal area is thought to contribute to this heating. If we compare the mantle shear velocity at the top of our model with those of pure shield models we obtain a reduction of 0.1–0.2 km s⁻¹, essentially 4.7–4.8 to 4.6 km s⁻¹. The

temperature difference for this velocity difference is 300°–600°, assuming that the upper mantle is composed of olivine (40 per cent), clinopyroxene and garnet as suggested by Duffy & Anderson (1989). We have $(d\beta/dT)_p = -3.3 \times 10^{-4} \text{ km s}^{-1} \text{ } ^\circ\text{C}^{-1}$ for upper mantle materials at 1000°K (Duffy, personal communication; Suzuki, Anderson & Sumino 1983). This temperature estimation is somewhat higher than the above estimates (see Molnar 1989), reflecting the contrast in velocity models (see Fig. 16), where Lyon-Caen's model has a higher lid velocity than TIP. Our results suggest that the crustal structure is playing a particularly important role in controlling the tectonics of the Tibetan Plateau and surrounding regions. Thus the higher resolution of this complex structure is essential and will be possible when the new digital observations from the Soviet Union and China become available.

In conclusion, we have examined some of the special problems associated with determining the upper mantle structure beneath Tibet. The principal difficulty is caused by the absence of stations located on the thickened plateau structure. This situation is compounded by inaccuracies in source locations and origin times for events in the region. We have attempted to quantify these effects by locating some master events, modelling teleseismic waveforms in shape and in timing, and by developing timing corrections based on 2-D numerical experiments. Our results indicate that P_n and S_n velocities from previous studies are probably 2–3 per cent too high based on geometrical corrections for laterally varying crustal structure. The most meaningful data in determining the structure directly beneath Tibet are from the SS–S observations. Near 50°, three distinct branches of SS appear; the slowest shows the shallowest bottoming and it is the timing of this particular phase that is the most diagnostic. Our results suggest that the separation of branches and relative timing are similar to that found in other shields and that the structure is shield-like below 200 km. However, the waveform consistency is poor, suggesting considerable crustal complexity. These features will be explored in future work.

ACKNOWLEDGMENTS

Dr Don L. Anderson reviewed the earlier version of the manuscript. The editor, Jeffrey Park and a few anonymous reviewers contributed many helpful comments for which we are grateful. This research was supported, by the National Science Foundation grant EAR-89-04767, and by the Advanced Research Projects Agency of the Department of Defense and was monitored by the Air Force Geophysical Laboratory under the contract F1962889K0028. Contribution no. 4733 from the Division of Geological and Planetary Sciences, California Institute of Technology, Pasadena, CA 91125.

REFERENCES

- Baranowski, H., Armbruster, H., Seeber, L. & Molnar, P., 1984. Focal depths and fault plane solutions of earthquakes and active tectonics of the Himalaya, *J. geophys. Res.*, **89**, 6919–6928.
- Barazangi, M. & Ni, J., 1982. Velocities and propagation characteristics of P_n and S_n beneath the Himalayan arc and Tibetan plateau: possible evidence for underthrusting of Indian continental lithosphere beneath Tibet, *Geology*, **10**, 179–185.
- Brandon, C. & Romanowicz, B., 1986. A 'no-lid' zone in the central Chang-Thang platform of Tibet: Evidence from pure path phase velocity measurements of long period Rayleigh waves, *J. geophys. Res.*, **B6**, 6547–6564.
- Chapman, C. H., 1978. A new method for computing synthetic seismograms, *Geophys. J. R. astr. Soc.*, **57**, 649–70.
- Chen, Wang-Ping & Molnar, P., 1981. Constraints on the seismic wave velocity structure beneath the Tibetan Plateau and their tectonic implications, *J. geophys. Res.*, **86**, 5937–5962.
- Chun, Kin-yip & McEvelly, T. V., 1985. New seismological evidences of Tibetan lithosphere structure, *Acta Geophysica Sinica*, **28**, Suppl. I., 135–147 (in Chinese, English abstract).
- Duffy, T. S. & Anderson, D. L., 1989. Seismic velocities in mantle minerals and the mineralogy of the upper mantle, *J. geophys. Res.*, **94**, 1895–1912.
- Dziewonski, A. M. & Anderson, D. L., 1983. Travel times and station corrections for P waves at teleseismic distances, *J. geophys. Res.*, **88**, 3295–3314.
- Feng, C., 1982. A surface wave study of crustal and upper mantle structures of Eurasia, *PhD thesis*, University of Southern California.
- Grand, S. P. & Helmberger, D. V., 1984a. Upper mantle shear structure of North America, *Geophys. J. R. astr. Soc.*, **76**, 399–438.
- Grand, S. P. & Helmberger, D. V., 1984b. Upper mantle shear structure beneath the northwest Atlantic Ocean, *J. geophys. Res.*, **89**, 11 465–11 475.
- Grand, S. P. & Helmberger, D. V., 1985. Upper mantle shear structure beneath Asia from multi-bounce S waves, *Phys. Earth planet. Inter.*, **41**, 154–169.
- Harkrider, D. G., 1964. Surface waves in multilayered elastic media, I. Rayleigh and Love waves from buried sources in a multilayered elastic half-space, *Bull. seism. Soc. Am.*, **54**, 627–679.
- Harkrider, D. G., 1970. Surface waves in multilayered elastic media, II. Higher mode spectra and spectral ratios from point sources in plane layered Earth models, *Bull. seism. Soc. Am.*, **54**, 1937–1987.
- Helmberger, D. V. & Vidale, J. E., 1988. Modelling strong motions produced by earthquakes with two-dimensional numerical codes, *Bull. seism. Soc. Am.*, **78**, 109–121.
- Hirn, A. *et al.*, 1984. Crustal structure and variability of the Himalayan border of Tibet, *Nature*, **307**, 23–25.
- Holt, W. E. & Wallace, T. C., 1990. Crustal thickness and upper mantle velocities in the Tibetan Plateau region from the inversion of regional P_n waveforms: Evidence for a thick upper mantle lid beneath southern Tibet, *J. geophys. Res.*, **95**, 12 495–12 525.
- Langston, C. A., 1977. Corvallis, Oregon, crustal and upper mantle receiver structure from teleseismic P and S waves, *Bull. seism. Soc. Am.*, **67**, 713–724.
- Langston, C. A. & Helmberger, D. V., 1975. A procedure for modelling shallow dislocation sources, *Geophys. J. R. astr. Soc.*, **42**, 117–130.
- LeFevre, L. V. & Helmberger, D. V., 1989. Upper mantle P velocity of the Canadian Shield, *J. geophys. Res.*, **94**, 17 749–17 765.
- Ludwig, W. J., Nafe, J. E. & Drake, C. L., 1970. Seismic refraction, in *The Sea*, vol. 4, part I, pp. 53–84, ed. Maxwell, A. E., Wiley-Interscience, New York.
- Lyon-Caen, H., 1986. Comparison of the upper mantle shear wave velocity structure of the Indian Shield and the Tibetan Plateau and tectonic implications, *Geophys. J. R. astr. Soc.*, **86**, 727–749.
- Mallick, S. & Frazer, L. N., 1988. Rapid computation of multioffset vertical seismic profile synthetic seismograms for layered media, *Geophysics*, **55**, 479–491.

- Molnar, P., 1989. The geology evolution of the Tibetan Plateau, *Am. Sci.*, **77**, 350–360.
- Molnar, P. & Chen, W.-P., 1983. Focal depths and fault plane solutions of earthquakes under the Tibetan Plateau, *J. geophys. Res.*, **88**, 1180–1196.
- Minster, J. F., Jordan, T. J., Molnar, P. & Haines, E., 1974. Numerical modelling of instantaneous plate tectonics, *Geophys. J. R. astr. Soc.*, **36**, 541–576.
- Ni, J. & Barazangi, M., 1983. High frequency seismic wave propagation beneath the Indian Shield, Himalayan arc, Tibetan Plateau and surrounding regions: High uppermost mantle velocities and efficient *Sn* propagation beneath Tibet, *Geophys. J. R. astr. Soc.*, **72**, 665–681.
- Ni, J. & Barazangi, M., 1984. Seismotectonics of the Himalayan collision zone: geometry of the underthrusting Indian plate beneath the Himalaya, *J. geophys. Res.*, **89**, 1147–1163.
- Rial, J. A., Grand, S. & Helmberger, D. V., 1984. A note on lateral variation in upper mantle shear-wave velocity across the Alpine front, *Geophys. J. R. astr. Soc.*, **77**, 639–654.
- Romanowicz, B. A., 1982. Constraints on the structure of the Tibet Plateau from pure path phase velocities of Love and Rayleigh waves, *J. geophys. Res.*, **87**, 6865–6883.
- Romanowicz, B. A., 1984. Pure path attenuation measurements of long-period Rayleigh waves across the Tibet Plateau, *Phys. Earth planet. Inter.*, **36**, 116–123.
- Shedlock, K. M. & Roecker, S. W., 1987. Elastic wave velocity structure of the crust and upper mantle beneath the North China basin, *J. geophys. Res.*, **92**, 9327–9350.
- Singh, D. D., 1977. Crust and upper mantle velocity structure beneath north and central India from the phase and group velocity of Rayleigh and Love waves, *Tectonophysics*, **139**, 187–203.
- Suzuki, I., Anderson, O. L. & Sumino, Y., 1983. Elastic properties of a single-crystal forsterite Mg_2SiO_4 , up to 1200 K, *Phys. Chem. Min.*, **10**, 38–46.
- Tapponnier, P. & Molnar, P., 1977. Active faulting and tectonics of China, *J. geophys. Res.*, **82**, 2905–2930.
- Teng, Ji-Wen, 1987. Explosion study of the structure and seismic velocity distribution of the crust and upper mantle under the Xizang (Tibet) Plateau, *Geophys. J. R. astr. Soc.*, **89**, 405–414.
- Wang, Shu-Yun & Xu, Zhong-Huai, 1985. Seismic tectonic stress fields of eastern continental China, *Acta Seismological Sinica*, **7**, 17–31 (in Chinese, figure captions in English).
- Wang, Kai & Yao, Zhen-Xing, 1989. Preliminary study of upper mantle shear velocity structure of China, *Chinese J. Geophys.*, **32**, 49–60 (English edition published by Allerton Press Inc., New York).
- Wier, S., 1982. Surface wave dispersion and earth structure in south-eastern China, *Geophys. J. R. astr. Soc.*, **69**, 33–47.
- Yang, Zunyi, Cheng, Yuqi & Wang, Hongzhen, 1986. *The Geology of China, Oxford Monographs on Geology and Geophysics*, vol. 3, Clarendon Press, Oxford.
- Zhang, Zh. M., Liou, J. G. & Coleman, R. G., 1984. An outline of the plate tectonics of China, *Geol. Soc. Am. Bull.*, **5**, 295–312.